



When MoS₂ meets FeOOH: A “one-stone-two-birds” heterostructure as a bifunctional electrocatalyst for efficient alkaline water splitting

Meiyong Zheng^{a,b}, Kailu Guo^a, Wen-Jie Jiang^{b,*}, Tang Tang^{b,c}, Xuyan Wang^a, Panpan Zhou^a, Jing Du^a, Yongqing Zhao^a, Cailing Xu^{a,**}, Jin-Song Hu^{b,c,*}

^a State Key Laboratory of Applied Organic Chemistry, Laboratory of Special Function Materials and Structure Design of the Ministry of Education, College of Chemistry and Chemical Engineering, Lanzhou University Lanzhou 730000, China

^b Beijing National Laboratory for Molecular Sciences (BNLMS), CAS Key Laboratory of Molecular Nanostructure and Nanotechnology, Institute of Chemistry, Chinese Academy of Sciences, Beijing 100190, China

^c School of Chemical Sciences, University of Chinese Academy of Sciences, Beijing 100049, China

ARTICLE INFO

Keywords:

Bifunctional electrocatalysts
Electronic modulation
Oxygen evolution reaction
Hydrogen evolution reaction
Water splitting

ABSTRACT

MoS₂ has emerged as an attractive electrocatalyst for hydrogen evolution reaction (HER) although its performance still needs to be further enhanced, especially in alkaline solution due to inferior ability for water dissociation. Herein, we discover that coupling water-dissociation-active FeOOH with MoS₂ grown on Ni₃S₂ nanowire arrays to achieve a core-shell Ni₃S₂@MoS₂/FeOOH heterostructure can not only significantly accelerate the HER of MoS₂, but also appreciably promote the OER activity of the catalyst. Systematic investigations on Ni₃S₂@MoS₂/FeOOH and a series of delicately designed control catalysts reveal that such synergistically enhanced electrocatalytic performance for both OER and HER should be ascribed to the coupling effect and electronic modulation between FeOOH and MoS₂. As a result, the prepared Ni₃S₂@MoS₂/FeOOH exhibits small overpotentials of 95 mV for HER and 234 mV for OER at 10 mA cm⁻². The alkaline electrolyzer using it as both anode and cathode only need a cell voltage of 1.57 V to output a stable current density of 10 mA cm⁻², enabling it as an efficient bifunctional electrocatalyst for alkaline overall water splitting. The present strategy opens up opportunities to develop new efficient electrocatalysts for diverse applications by coupling OER-active electron-modulating component with highly-active HER electrocatalyst or vice versa.

1. Introduction

Electrochemical water splitting has been regarded as one of the most favorable ways to mass produce hydrogen for the alternative and clean renewable energy [1]. The non-precious metal electrocatalysts with high catalytic activity and durability are desperately needed due to the sluggish dynamic process of hydrogen evolution reaction (HER) [2] and oxygen evolution reaction (OER) [3,4]. Especially, a bifunctional electrocatalyst with high catalytic activity for both HER and OER in an integrated electrolyzer is urgently demanded because it can decrease the catalyst costs, simplify the complexity of system, and avoid the mismatch of pH ranges [5,6]. To date, the state-of-the-art electrocatalysts of water splitting are still the precious metal-based materials such as Pt, IrO₂, and RuO₂. However, the scarcity and high cost seriously hinder their widespread application in commercial electrolyzer. Thus, different earth-abundant electrocatalysts

have been explored over the past decades such as transition metal oxides [7,8], hydroxides [9,10], carbides [11–13], nitrides [14,15], selenides [16,17], phosphides [18], sulfides [19,20] and so on. Although great progress has been made in this field, high potential (i.e. > 1.60 V at 10 mA cm⁻²) is still needed for overall water splitting [21]. In view of the requirements in practical water-alkali and chlor-alkali electrolyzes [22], the bifunctional electrocatalysts with low overpotentials for both HER and OER in alkaline solution are very imperative and important.

Recently, MoS₂ has received intensive studies owing to its elemental abundance, the electron-transfer-favoring layered structure, and excellent electrochemical stability and activities [23,24]. It commonly shows the favorable activity for HER in acidic electrolyte due to the near-optimal hydrogen adsorption free energy [25]. However, the HER kinetics on MoS₂ in alkaline condition is sluggish. The HER process in alkaline medium generally includes: Volmer step where water dissociation

* Corresponding authors at: Beijing National Laboratory for Molecular Sciences (BNLMS), CAS Key Laboratory of Molecular Nanostructure and Nanotechnology, Institute of Chemistry, Chinese Academy of Sciences, Beijing 100190, China.

** Corresponding author at: State Key Laboratory of Applied Organic Chemistry, Laboratory of Special Function Materials and Structure Design of the Ministry of Education, College of Chemistry and Chemical Engineering, Lanzhou University Lanzhou 730000, China.

E-mail addresses: jiangwenjie@iccas.ac.cn (W.-J. Jiang), xucl@lzu.edu.cn (C. Xu), hujs@iccas.ac.cn (J.-S. Hu).

<https://doi.org/10.1016/j.apcatb.2018.12.019>

Received 15 September 2018; Received in revised form 30 November 2018; Accepted 6 December 2018

Available online 06 December 2018

0926-3373/ © 2018 Elsevier B.V. All rights reserved.

occurs to form reactive adsorbed hydrogen H_{ad} ($H_2O + M + e^- \rightleftharpoons M-H_{ad} + OH^-$), followed by either Heyrovsky step ($H_2O + M-H_{ad} + e^- \rightleftharpoons M + H_2 + OH^-$) or Tafel recombination step ($2M-H_{ad} \rightleftharpoons 2M + H_2$) [22]. The poor catalytic activity of MoS_2 for alkaline HER is attributed to its low efficiency in splitting water into H_{ad} [23,26]. Therefore, in order to promote the alkaline HER on MoS_2 based catalysts, it is crucial to modulate its electronic structure or couple other components to accelerate water dissociation. A couple of strategies have been investigated and witnessed the enhanced alkaline HER activity. For example, heteroatom (Co, Ni) doping to promote water dissociation and interface engineering to modulate the electronic structure have been proved to be able to enhance the intrinsic HER catalytic activity on MoS_2 [27–30]. The introduction of secondary components such as MoS_2/Ni_3S_2 and MoS_2/Co_9S_8 heterostructures have also been reported to improve the electrocatalytic activity of MoS_2 [31–33]. Although the great progress has been made in this aspect, the alkaline HER activity of MoS_2 -based catalysts still needs to be further enhanced. Especially, to further advance their application in electrochemical water splitting, exploring feasible strategies to simultaneously modulate both HER and OER activity of MoS_2 -based materials and make them as efficient bifunctional electrocatalysts would be highly desirable.

Compared with Co and Ni-based materials, FeOOH shows much stronger adsorption of hydroxyl species, enabling it effective for water dissociation [26,34–37]. Unfortunately, the OER activity of FeOOH is much inferior to Ni and Co-based materials because of its too strong interaction with hydroxyl species [26]. Herein, we discover that coupling FeOOH with MoS_2 can not only promote the alkaline HER activity of MoS_2 by accelerating water dissociation, but also enhance the OER activity of FeOOH through the electronic modulation from MoS_2 . Such “one-stone-two-birds” effect enables the hybrid of $MoS_2/FeOOH$ as an efficient bifunctional electrocatalysts for overall electrochemical water splitting. To increase the density of active sites and facilitate electron transport and mass transfer, such coupled $MoS_2/FeOOH$ are fabricated on three-dimensional (3D) Ni_3S_2 nanowires on conductive Ni foam. As a result, the hybrid $Ni_3S_2@MoS_2/FeOOH$ exhibits much enhanced electrocatalytic activity for both alkaline HER and OER with overpotentials of 95 mV for HER and 234 mV for OER at 10 mA cm^{-2} . Benefited from the unique hierarchical heterostructure and dual functions, the alkaline electrolyzer using $Ni_3S_2@MoS_2/FeOOH$ as both anode and cathode deliver a stable current density of 10 mA cm^{-2} at only 1.57 V in overall water splitting.

2. Experimental section

2.1. Materials

All chemicals, including sodium molybdate dehydrate ($Na_2MoO_4 \cdot 2H_2O$), thioacetamide (CH_3CSNH_2), iron (III) nitrate nonahydrate ($Fe(NO_3)_3 \cdot 9H_2O$), diammonium oxalate monohydrate ($(NH_4)_2C_2O_4 \cdot H_2O$), sodium chloride (NaCl), sodium thiosulfate pentahydrate ($Na_2S_2O_3 \cdot 5H_2O$), acetone and ethanol, were purchased from Sigma-Aldrich in analytical grade (AR) and used without any further purification. Platinum (20 wt% on carbon black) and iridium dioxide (IrO_2) were purchased from Alfa Aesar and Sigma-Aldrich, respectively. Nickel foam (thickness: 1.6 mm, pore density: 110 ppi) was obtained from Changsha Keliyuan. Carbon cloth was purchased from the J & K Chemical Technology and washed sequentially with acetone, ethanol and water before use.

2.2. Synthesis of $Ni_3S_2@MoS_2$ heterostructure

$Ni_3S_2@MoS_2$ nanowires grown on Ni foam was synthesized through a facile hydrothermal method [33]. In a typical synthesis, 45 mg $Na_2MoO_4 \cdot 2H_2O$ and 90 mg thioacetamide were dissolved in 30 mL deionized water to obtain a uniform solution under continuous magnetic stirring for 30 min at room temperature. Afterwards, the obtained solution was transferred into a 50 mL Teflon-lined stainless-steel autoclave. A piece of Ni foam (NF), cleaned sequentially with acetone, ethanol and water,

was immersed into the above solution. The autoclave was then sealed and heated to 200°C for 24 h. After cooling down to room temperature, the resulting materials were rinsed with deionized water and ethanol several times and dried at 60°C .

2.3. Synthesis of Ni_3S_2

For comparative study, Ni_3S_2 nanowires grown on Ni foam was prepared according to the previous literature [38]. In brief, a piece of Ni foam was immersed into 30 mL solution containing 0.8 mmol $Na_2S_2O_3 \cdot 5H_2O$. The hydrothermal reaction was carried out at 140°C for 8 h to obtain Ni_3S_2 nanowires on Ni foam with a comparable ECSA with $Ni_3S_2@MoS_2$.

2.4. Synthesis of $Ni_3S_2@MoS_2/FeOOH$ hybrid

The FeOOH nanosheets were electrodeposited on $Ni_3S_2@MoS_2$ nanowires to form $Ni_3S_2@MoS_2/FeOOH$ hybrid in a mixed solution of $Fe(NO_3)_3 \cdot 9H_2O$, $(NH_4)_2C_2O_4 \cdot H_2O$, and NaCl at room temperature. To obtain the optimal electrochemical performance, different electrolyte concentrations (1.0, 2.0 or 3.0 mM $Fe(NO_3)_3 \cdot 9H_2O$; 2.5, 5.0 or 7.5 mM $(NH_4)_2C_2O_4 \cdot H_2O$; and 1.0, 2.0 or 3.0 mM NaCl), different current densities of electrodeposition (1, 2, and 3 mA cm^{-2}), and different electrodeposition time (5, 10 and 15 min) were conducted at room temperature. A Pt plate and a saturated calomel electrode (SCE) were utilized as the counter electrode and reference electrode, respectively. The obtained samples were washed with deionized water and dried at 60°C . For comparison, $Ni_3S_2/FeOOH$, NF/FeOOH and CC/FeOOH were prepared by directly electrodepositing FeOOH on Ni_3S_2 NWs-NF, Ni foam, and carbon cloth at the same conditions as above.

2.5. Material characterizations

X-Ray diffraction (XRD) patterns of the samples were obtained on a Rigaku D/M ax-2400 at a scanning rate of 10° min^{-1} over a 2θ range of $10\text{--}80^\circ$. The surface morphology of samples was characterized on a Hitachi S-4800 field-emission scanning electron microscope (FESEM) and a TecnaiTM G2 F30 transmission electron microscope (TEM). The chemical composition and element distribution were investigated with the energy dispersive X-ray spectroscopy (EDS). X-ray photoelectron spectroscopy (XPS) data were collected through a VGESCALAB MKII X-ray photoelectron spectrometer with a Mg-K α excitation source (1253.6 eV).

2.6. Electrochemical measurements

The electrochemical experiments were performed on a CHI760E electrochemical workstation equipped with a three-electrode configuration. Specifically, the as-prepared samples were directly used as the working electrode, a standard Hg/HgO electrode and a graphite rod were used as the reference and counter electrodes, respectively. The cyclic voltammetry and the linear sweep voltammetry curves were obtained at a scan rate of 5 mV s^{-1} in 1.0 M KOH aqueous solution. The potentials used in this work were converted to E_{RHE} according to the Nernst equation:

$$E_{RHE} = E_{Hg/HgO} + 0.059\text{ pH} + 0.098$$

For comparison, Pt/C (20 wt%) and IrO_2 electrodes (loaded on nickel foam with 2.0 mg cm^{-2}) were prepared via a drop coating method. To be more specific, 2.0 mg Pt/C (20%) or IrO_2 was dispersed in 1.0 mL deionized water, afterwards, the solution was dripped to a Ni foam ($1 \times 1\text{ cm}^2$) under a baking lamp. The electrochemical double layer capacitance C_{dl} of the materials were obtained through a series of cyclic voltammetry measurements at various scan rates (20, 40, 60, 80 and 100 mV s^{-1}) in the non-faradaic potential region from 0.924 to 1.024 V vs. RHE. The derived linear slope was calculated as C_{dl} . The impedance spectra (EIS) were recorded in an AC potential frequency range of 100000–0.01 Hz with an amplitude of

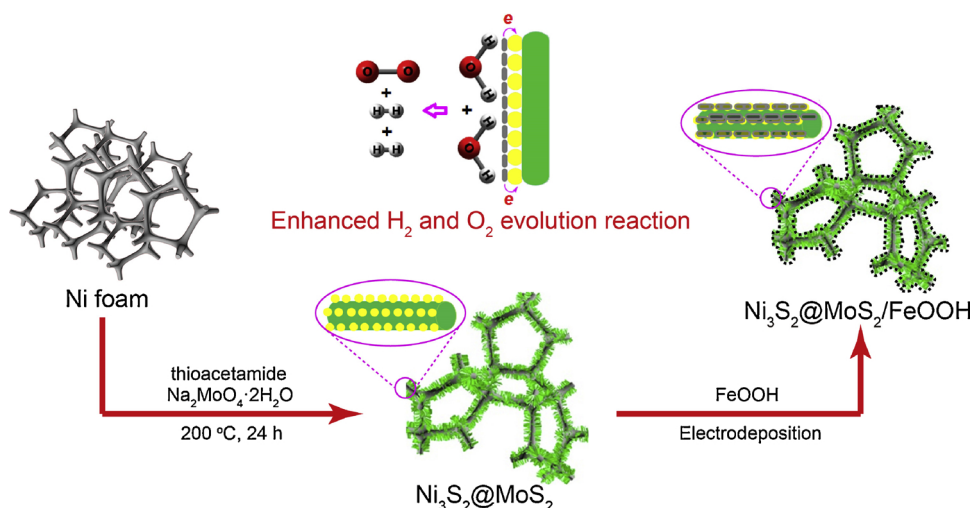
5 mV in 1.0 M KOH. All the curves displayed in this work were corrected against the iR compensation.

3. Results and discussions

3.1. Preparation and characterizations

As shown in Scheme 1, few-layer MoS₂ nanosheets decorated Ni₃S₂ nanowire arrays (Ni₃S₂@MoS₂) were firstly grown on Ni foam via a

hydrothermal method. Electrodeposition was then carried out to couple FeOOH on Ni₃S₂@MoS₂ (Ni₃S₂@MoS₂/FeOOH) according to the modified method reported in literatures [39,40]. The electrodeposition conditions such as current density, deposition time, and electrolyte concentration etc. were finely tuned to optimize the status of coupled FeOOH, thus the catalytic performance of the hybrid catalyst. The products and control catalysts were firstly characterized by X-ray power diffraction (XRD) technique. XRD patterns of as-prepared Ni₃S₂, Ni₃S₂@MoS₂ and Ni₃S₂@MoS₂/FeOOH (Fig. 1a) on Ni foam display two set of



Scheme 1. Schematic illustration for the preparation of Ni₃S₂@MoS₂/FeOOH.

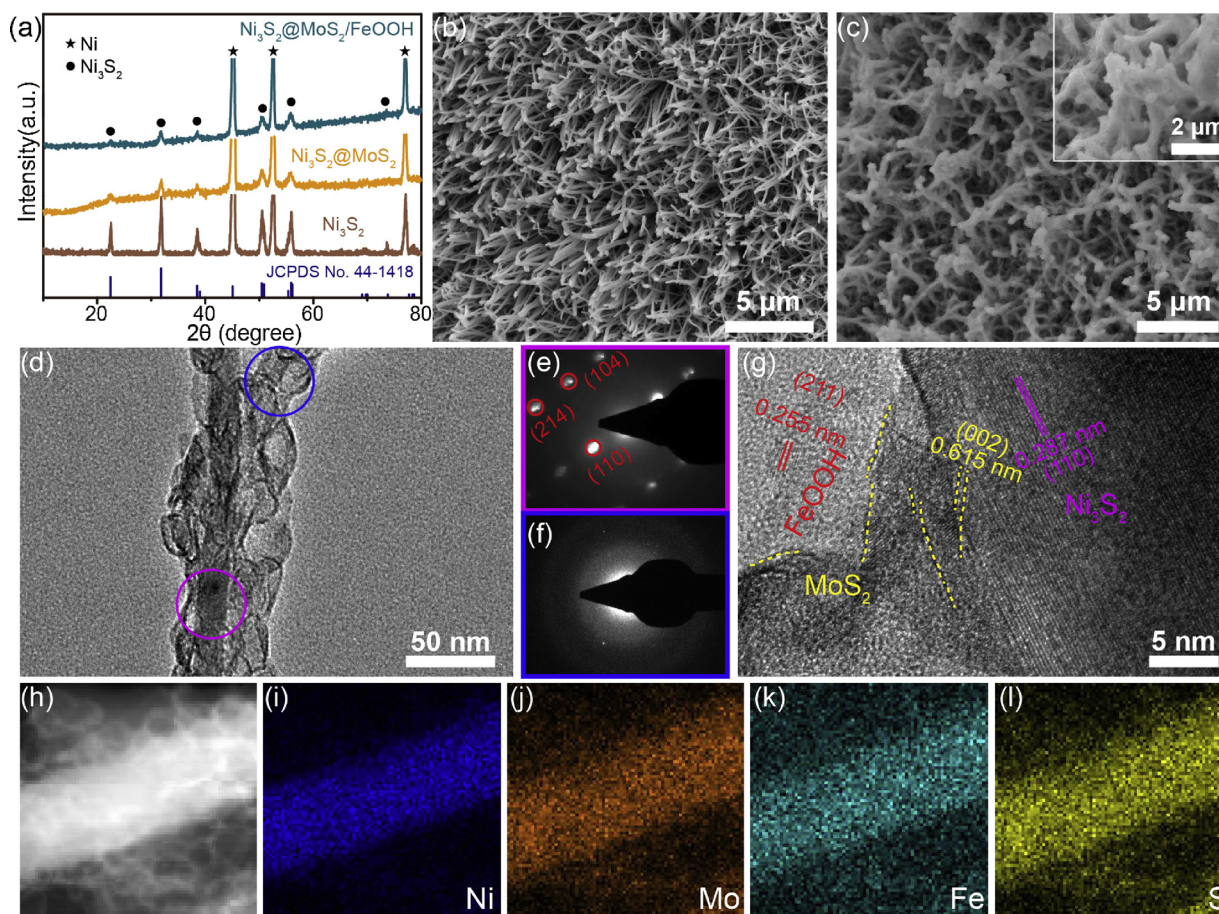


Fig. 1. (a) XRD patterns of as-prepared Ni₃S₂, Ni₃S₂@MoS₂, and Ni₃S₂@MoS₂/FeOOH. SEM images of (b) Ni₃S₂@MoS₂ and (c) Ni₃S₂@MoS₂/FeOOH. The inset in c is the enlarged SEM image of Ni₃S₂@MoS₂/FeOOH. (d) TEM image, (e–f) SAED patterns, (g) HRTEM image, and (h–l) elemental mapping images of Ni₃S₂@MoS₂/FeOOH.

signals: one assigned to metal Ni Foam substrate (JCPDS No. 65-2865) at 44.7° , 52.1° , 76.6° as indicated by pentagrams; the other assigned to hexagonal Ni_3S_2 (JCPDS No. 44-1418) at 21.9° , 31.3° , 38.1° , 49.9° , 55.4° , 69.3° , 73.2° , and 78.0° as indicated by dots [41]. No obvious diffraction peaks of MoS_2 and FeOOH are observed for $\text{Ni}_3\text{S}_2/\text{MoS}_2$ and $\text{Ni}_3\text{S}_2/\text{MoS}_2/\text{FeOOH}$, implying their low crystallinities. Notably, the relative intensity of Ni_3S_2 peaks significantly decreases for $\text{Ni}_3\text{S}_2/\text{MoS}_2$ and $\text{Ni}_3\text{S}_2/\text{MoS}_2/\text{FeOOH}$ because of the coverage of MoS_2 and FeOOH . Scanning electron microscope (SEM) images of $\text{Ni}_3\text{S}_2/\text{MoS}_2$ and $\text{Ni}_3\text{S}_2/\text{MoS}_2/\text{FeOOH}$ are shown in Fig. 1b and c, respectively. The morphology of nanowire arrays can be clearly observed for these two samples. However, the nanowires become thicker and the surfaces become rougher after the deposition of FeOOH (Fig. 1c), indicating the successful coupling of FeOOH on $\text{Ni}_3\text{S}_2/\text{MoS}_2$. Moreover, the energy dispersive spectroscopic (EDS) results confirm the existence of Mo, Ni, and S elements in $\text{Ni}_3\text{S}_2/\text{MoS}_2$ as well as Mo, Ni, S, Fe, and O elements in $\text{Ni}_3\text{S}_2/\text{MoS}_2/\text{FeOOH}$ (Fig. S1). The typical TEM image of single nanowire clearly shows a core-shell structure with a nanowire core in a diameter of about 20 nm and sheet-like nanostructure shell (Fig. 1d). The selected-area electron diffraction (SAED) patterns collected on Ni_3S_2 nanowire (indicated by purple circle in Fig. 1d) and $\text{MoS}_2/\text{FeOOH}$ (indicated by blue circle in Fig. 1d) are shown in Fig. 1e and 1f, respectively. Well-defined diffraction pattern on nanowire agrees well with the hexagonal Ni_3S_2 , corroborating the core is single-crystalline Ni_3S_2 nanowire. While the diffusive diffraction on shell imply that the $\text{MoS}_2/\text{FeOOH}$ shell could be amorphous or in low crystallinity, which is consistent with XRD results. Such heterostructures of $\text{Ni}_3\text{S}_2/\text{MoS}_2/\text{FeOOH}$ are further confirmed by high-resolution TEM image (HRTEM, Fig. 1g). The continuous lattice fringes with a distance of 0.287 nm are well indexed to the (110) planes of Ni_3S_2 . The indistinct lattice fringes with a distance of 0.615 nm (marked by yellow dash line) are the typical feature for the (002) planes of MoS_2 . On the outmost shell part,

continuous lattice fringes in short range with a distance of 0.255 nm is observed, which can be assigned to the second strongest diffraction peak of (211) planes of FeOOH . This result suggests the electrodeposited FeOOH is not well crystallized, consistent with previous reports using similar synthetic method [39,40]. It should be noted that such FeOOH outlayer are intimately grown on MoS_2 nanosheets during all TEM observations. Scanning TEM image in Fig. 1h more clearly reveals the heterostructure of nanowire core and nanosheet shell. The elemental mapping images in Fig. 1i–l corroborate such heterostructure with Ni mainly on nanowire while Fe, Mo and S in the whole region.

3.2. Electronic interaction analyses

The potential electronic interaction of FeOOH , MoS_2 , and Ni_3S_2 is explored by X-ray photoelectron spectroscopy (XPS). For comparison, FeOOH was also electrodeposited on carbon cloth (denoted as CC/ FeOOH) by the same procedure. The XPS survey spectra (Fig. S2a) clearly show that the presence of Fe and O elements for CC/ FeOOH , and Mo, Ni, S, Fe, and O elements for $\text{Ni}_3\text{S}_2/\text{MoS}_2/\text{FeOOH}$. In Fig. 2a, the Fe 2p XPS profile for $\text{Ni}_3\text{S}_2/\text{MoS}_2/\text{FeOOH}$ is similar to that for CC/ FeOOH except for the positively shifted Fe $2p_{3/2}$ peak of 0.5 eV, suggesting the electron density redistribution of FeOOH on $\text{Ni}_3\text{S}_2/\text{MoS}_2$ and their potential electronic interaction [42]. In O 1s XPS spectra (Fig. 2b), the typical features of lattice O^{2-} (530.7 eV), OH^- (531.3 eV) coming from adsorbed species or electrodeposited FeOOH , and adsorbed water (532.2 eV) can be clearly resolved for both CC/ FeOOH and $\text{Ni}_3\text{S}_2/\text{MoS}_2/\text{FeOOH}$. The Fe 2p and O 1s XPS spectra corroborate the formation of FeOOH [43]. The Mo 3d XPS spectra for $\text{Ni}_3\text{S}_2/\text{MoS}_2$ and $\text{Ni}_3\text{S}_2/\text{MoS}_2/\text{FeOOH}$ are shown in Fig. 2c. The peak at 231.8 eV for $\text{Ni}_3\text{S}_2/\text{MoS}_2$ can be well indexed to the Mo $3d_{3/2}$ of Mo^{4+} , typical feature of MoS_2 . A pair of peaks at 232.2 and 235.4 eV are attributed to the oxidation of Mo species (Mo^{6+}), which are commonly observed in

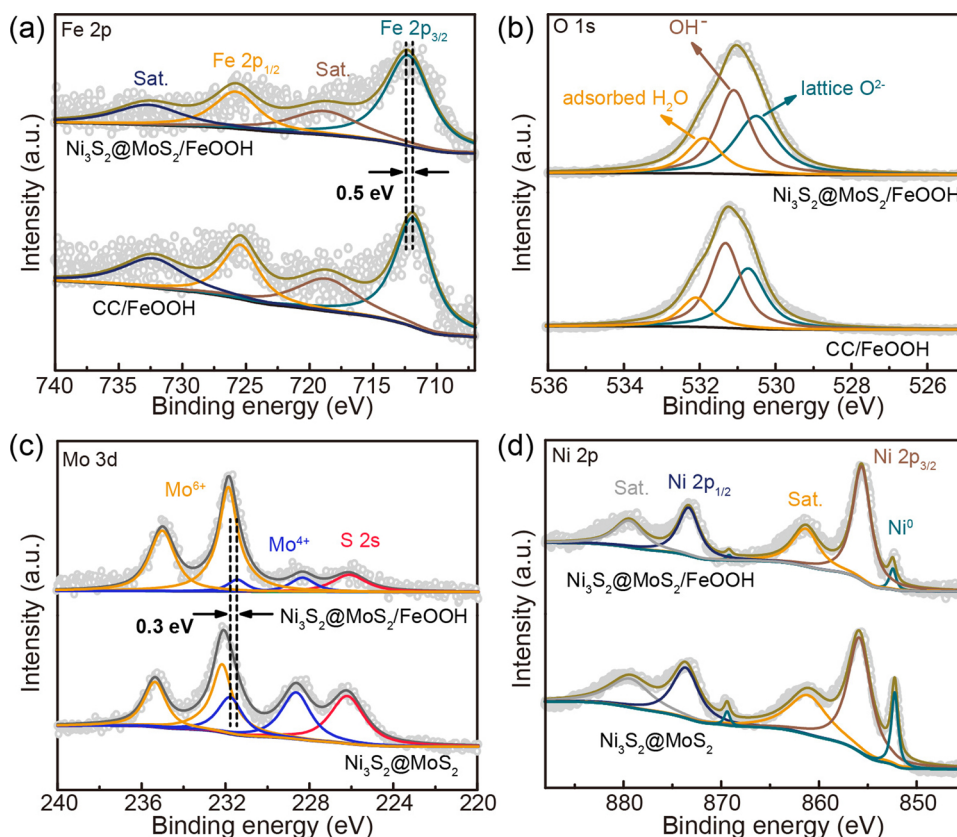


Fig. 2. (a) Fe 2p and (b) O 1s XPS spectra of $\text{Ni}_3\text{S}_2/\text{MoS}_2/\text{FeOOH}$ and FeOOH on carbon cloth (FeOOH/CC). (c) Mo 3d and (d) Ni 2p XPS spectra of $\text{Ni}_3\text{S}_2/\text{MoS}_2/\text{FeOOH}$ and $\text{Ni}_3\text{S}_2/\text{MoS}_2$.

the Mo 3d spectra of MoS₂ [44,45]. In contrast, the Mo 3d_{3/2} peak of Mo⁴⁺ for Ni₃S₂@MoS₂/FeOOH shows a negative shift of about 0.3 eV, indicating the electron transfer from Fe atoms to Mo atoms. The similar binding energy shift could also be observed on FeOOH directly on MoS₂ (MoS₂/FeOOH) as shown in Fig. S3. Such electronic modulation on both Fe and Mo centers in Ni₃S₂@MoS₂/FeOOH heterostructure would be favorable for improving their HER and OER activity according to the previous reports that lower valence state of Mo in MoS₂ shows higher HER activity and the higher valence state of Fe in FeOOH shows higher OER activity [46,47]. The coexistence of Ni⁺ and Ni²⁺ in Ni₃S₂@MoS₂ and Ni₃S₂@MoS₂/FeOOH is evidenced by the Ni 2p_{3/2} peaks at about 852.3 and 855.9 eV, respectively, which can be attributed to Ni₃S₂ phase (Fig. 2d) [48]. No obvious shift of binding energy for Ni species in Ni₃S₂@MoS₂/FeOOH is discovered, indicating the weak electron interaction between FeOOH and Ni₃S₂. The S 2p_{3/2} spectra of both samples exhibit the typical sulfur configuration in metal sulfides, corresponding to Ni₃S₂ or MoS₂ (Fig. S2b).

3.3. Electrocatalytic activity and kinetics for HER and OER

The electrochemical performances for water splitting of Ni₃S₂@MoS₂/FeOOH and control catalysts (Ni₃S₂@MoS₂ and Ni₃S₂@FeOOH) were evaluated in 1.0 M KOH solution. To obtain the optimal electrochemical activity of Ni₃S₂@MoS₂/FeOOH, the electrodeposition conditions including current density, time, and electrolyte concentration were systemically investigated as shown in Fig. S4–S6. It can be seen that the optimal electrodeposition current density is 2 mA cm⁻², the optimal electrolyte concentration is 2 mM, and the optimal electrodeposition time is 10 min. In addition, to explore the role of each component for catalyzing HER and OER, FeOOH was also electrodeposited on Ni foam and Ni₃S₂ nanowires using the optimal electrodeposition recipe. The obtained samples are denoted as NF/FeOOH and Ni₃S₂/FeOOH, respectively. The commercial IrO₂ nanoparticles and commercial Pt/C casted on Ni foam were also evaluated for

comparison. The catalytic activities of these catalysts for OER are shown in Fig. 3a. The obvious peak with an onset potential of about 1.35 V is the oxidation of nickel species [49]. Considering the strong oxidation peak, the overpotential at 10 mA cm⁻² (η_{10}) is given by the reverse scan of cyclic voltammetry (CV) at 5 mV s⁻¹ according to the literatures [31,50]. As seen in Fig. 3a, Ni₃S₂@MoS₂ shows the worst OER activity with a large η_{10} of 310 mV. This value can be reduced to 260 mV for Ni₃S₂/FeOOH, which is due to the well-known higher intrinsic OER activity of FeOOH than MoS₂. However, the η_{10} can be further decreased to 234 mV on Ni₃S₂@MoS₂/FeOOH, which is far lower than 311 mV for NF/FeOOH and 280 mV for commercial IrO₂ (Fig. S7). Impressively, Ni₃S₂@MoS₂/FeOOH can exhibit a very low overpotential of 282 mV to reach a high current density of 100 mA cm⁻². Such outstanding catalytic activity of Ni₃S₂@MoS₂/FeOOH for OER surpasses many reported Fe-based and even NiFe-based electrocatalysts (Table S1). Besides, it exhibits the lowest Tafel slope of 49 mV dec⁻¹ (Fig. 3b), which is lower than Ni₃S₂/FeOOH (56 mV dec⁻¹) and Ni₃S₂@MoS₂ (114.0 mV dec⁻¹). This value is even smaller than those of reported highly-active OER catalysts [51,52], indicating the excellent reaction kinetics on Ni₃S₂@MoS₂/FeOOH. These results suggest that the coupling FeOOH on MoS₂ efficiently enhances the OER activity of FeOOH.

The HER activities of these catalysts are further evaluated as shown in Fig. 3c and Fig. S8. The Ni₃S₂/FeOOH exhibits a η_{10} of 189 mV, lower than 228 mV for NF/FeOOH. Besides, the η_{10} of Ni₃S₂ nanorods on NF (denoted as NF/Ni₃S₂) is 210 mV. These results suggest the low activity of FeOOH and Ni₃S₂ for HER. However, the η_{10} value can be decreased to 134 mV for Ni₃S₂@MoS₂, which is attributed to the well-known high intrinsic activity of MoS₂ for HER. As expected, the lowest η_{10} of 95 mV can be achieved on Ni₃S₂@MoS₂/FeOOH heterostructure, superior to those of reported MoS₂/Ni₃S₂ (110 mV) [50], MoS₂-CPs (186 mV) [53], and MoS₂/Mo (168 mV) [45], etc. Furthermore, Ni₃S₂@MoS₂/FeOOH can output the current density of 100 mA cm⁻² at a low overpotential of 177 mV, demonstrating its fast reaction kinetics and structural

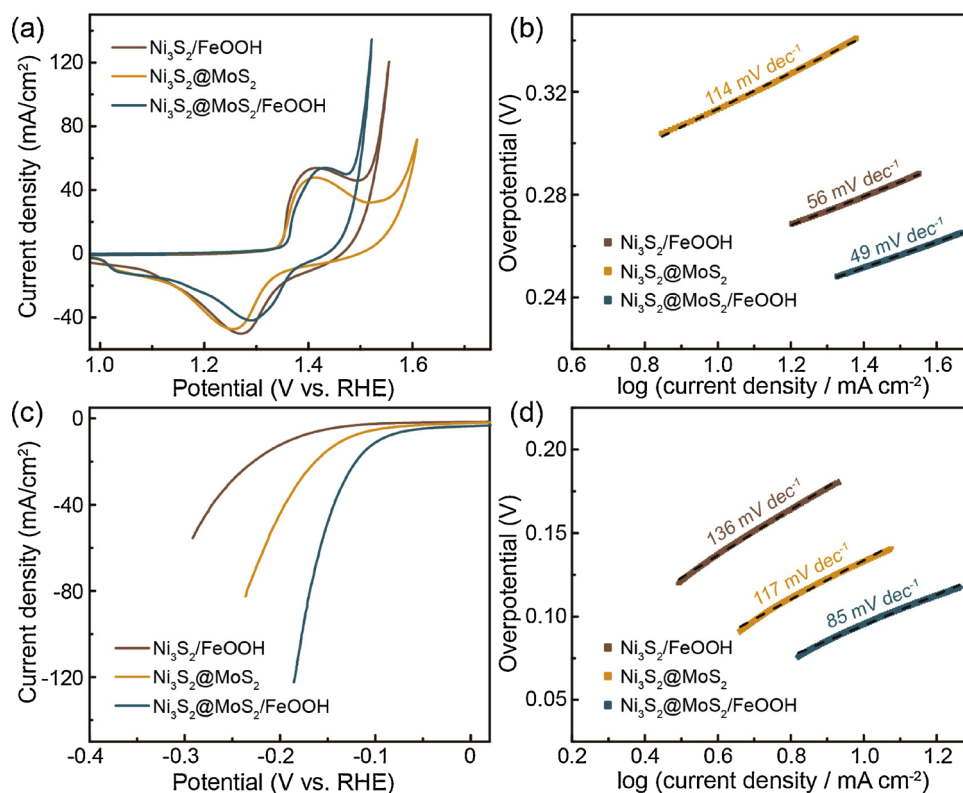


Fig. 3. (a) CV curves for OER at a scan rate of 5 mV s⁻¹ and (b) the corresponding Tafel plots, recorded on Ni₃S₂/FeOOH, Ni₃S₂@MoS₂, and Ni₃S₂@MoS₂/FeOOH. (c) Polarization curves for HER at a scan rate of 5 mV s⁻¹ and (d) the corresponding Tafel plots, recorded on Ni₃S₂/FeOOH, Ni₃S₂@MoS₂, and Ni₃S₂@MoS₂/FeOOH.

advantages. In addition, the Tafel slope of $\text{Ni}_3\text{S}_2/\text{MoS}_2/\text{FeOOH}$ drops down to 85 mV dec^{-1} (Fig. 3d) from 136 mV dec^{-1} for $\text{Ni}_3\text{S}_2/\text{FeOOH}$ and 117 mV dec^{-1} for $\text{Ni}_3\text{S}_2/\text{MoS}_2$, suggesting the more favorable HER kinetics after the introduction of FeOOH on $\text{Ni}_3\text{S}_2/\text{MoS}_2$. As mentioned in the Introduction, the HER kinetics depends on the balance between the dissociation of adsorbed water (Volmer reaction) and the interaction of hydrogen atom and hydroxyl ions with the active sites [22]. The previous experimental and theoretical results indicate that the alkaline HER rate is mainly dominated by the dissociation of adsorbed water molecule due to the high activation energy, which is further controlled by the chemisorption energies of hydrogen atom and hydroxyl ions [54,55]. The too strong chemisorption energies of hydroxyl ions could reduce the rate of desorption of OH_{ad} , which will affect the re-adsorption of H_2O on the surface of catalysts. When Volmer reaction is the rate-determining step, the corresponding Tafel slope was 120 mV dec^{-1} , while Heyrovsky process has a Tafel slope of 40 mV dec^{-1} and the Tafel slope of Tafel reaction is 30 mV dec^{-1} [56]. The Tafel slope of 85 mV dec^{-1} for $\text{Ni}_3\text{S}_2/\text{MoS}_2/\text{FeOOH}$ suggests that the rate-determining step might be Tafel process. Although the specific reaction mechanism could not be merely deduced through the Tafel slope, the distinct decrease of Tafel slope for $\text{Ni}_3\text{S}_2/\text{MoS}_2/\text{FeOOH}$ demonstrates the promoted Volmer reaction rate of HER. These results indicate that the coupling of MoS_2 and FeOOH can effectively promote the dissociation of adsorbed water through tuning adsorption energies of hydrogen atom and hydroxyl ions.

3.4. Origin of catalytic activity for HER and OER

To further explore the origin of the superior electrocatalytic activities of $\text{Ni}_3\text{S}_2/\text{MoS}_2/\text{FeOOH}$ for both HER and OER, the electrochemical active surface areas (ECSA) of all catalysts are firstly evaluated by testing electrochemical double layer capacitance (C_{dl}) in a non-Faradaic potential region (Figs. S9 and 4 a). The calculated C_{dl} of

$\text{Ni}_3\text{S}_2/\text{FeOOH}$ (7.30 mF cm^{-2}) is similar to that of $\text{Ni}_3\text{S}_2/\text{MoS}_2$ (7.73 mF cm^{-2}) and slightly lower than that of $\text{Ni}_3\text{S}_2/\text{MoS}_2/\text{FeOOH}$ (8.19 mF cm^{-2}) as shown in Fig. 4b, indicating that they have similar ECSAs and the improved electrochemical performance should not be from the slight differences in ECSA. The highest OER and HER activities of $\text{Ni}_3\text{S}_2/\text{MoS}_2/\text{FeOOH}$ should not be due to the increase of active sites, but the coupling interface and subsequent electronic interaction. It is reported that the interaction of intermediate species and 3d orbits of transition metal determines the OER activity of transition metal-based catalysts [57]. As evidenced by XPS measurements, the interaction between Ni atoms and Fe atoms in $\text{Ni}_3\text{S}_2/\text{MoS}_2/\text{FeOOH}$ heterostructure is weak. Therefore, the significant enhancement of OER activity from $\text{Ni}_3\text{S}_2/\text{FeOOH}$, $\text{Ni}_3\text{S}_2/\text{MoS}_2$ to $\text{Ni}_3\text{S}_2/\text{MoS}_2/\text{FeOOH}$ can be safely attributed to the electronic modulation of FeOOH by MoS_2 , which is evidenced by positive shift of $\text{Fe } 2p_{3/2}$ binding energy in $\text{Ni}_3\text{S}_2/\text{MoS}_2/\text{FeOOH}$ compared with that in $\text{Ni}_3\text{S}_2/\text{MoS}_2$. The charge transfer from FeOOH to MoS_2 could optimize the oxygen intermediate adsorption on the active sites, enhancing the OER activity [58]. Furthermore, MoS_2 exhibits the near-optimal hydrogen adsorption free energy but sluggish water dissociation process (Volmer step). The introduction of FeOOH can accelerate the water dissociation, improving HER kinetics of MoS_2 as demonstrated by much improved Tafel slope from 117 mV dec^{-1} for $\text{Ni}_3\text{S}_2/\text{MoS}_2$ to 85 mV dec^{-1} for $\text{Ni}_3\text{S}_2/\text{MoS}_2/\text{FeOOH}$. Such “one-stone-two-birds” effect between MoS_2 and FeOOH simultaneously optimizes the HER and OER process on $\text{Ni}_3\text{S}_2/\text{MoS}_2/\text{FeOOH}$ heterostructure. Moreover, electrochemical impedance spectra (EIS) were measured to understand the effect of HER and OER kinetics on catalytic activity. As shown in Fig. 4c–d, $\text{Ni}_3\text{S}_2/\text{MoS}_2/\text{FeOOH}$ exhibits the smallest semi-circular diameter for either HER or OER compared with $\text{Ni}_3\text{S}_2/\text{FeOOH}$, $\text{Ni}_3\text{S}_2/\text{MoS}_2$, suggesting the lowest charge-transfer resistance. It corroborates that coupling $\text{Ni}_3\text{S}_2/\text{MoS}_2$ with FeOOH results in the better reaction kinetics for HER and OER.

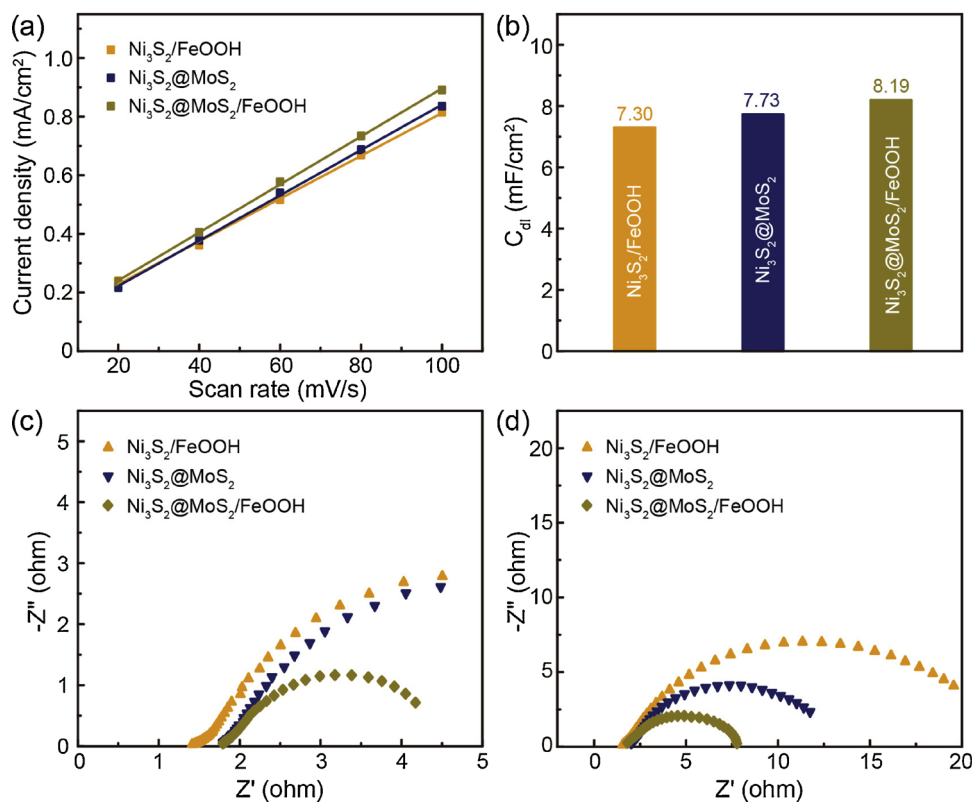


Fig. 4. (a) The plots of current density as a function of scan rates, (b) calculated C_{dl} values, (c) EIS spectra of OER at the overpotential of 230 mV, (d) EIS spectra of HER at the overpotential of 100 mV for $\text{Ni}_3\text{S}_2/\text{FeOOH}$, $\text{Ni}_3\text{S}_2/\text{MoS}_2$, and $\text{Ni}_3\text{S}_2/\text{MoS}_2/\text{FeOOH}$.

In order to further understand the catalytically active sites for HER and OER, more control samples including MoS_2 , FeOOH , and $\text{FeOOH}/\text{MoS}_2$ on carbon cloth were prepared and their catalytic activities for HER and OER were shown in Fig. S10. It can be seen that MoS_2 is almost inactive for OER and FeOOH is almost inactive for HER. That means the catalytic sites for HER and OER are MoS_2 and FeOOH , respectively.

3.5. Stability tests

The long-term durability is another key parameter to evaluate the practical application of electrocatalysts. Two methods were applied to assess the durability of our $\text{Ni}_3\text{S}_2@\text{MoS}_2/\text{FeOOH}$ for HER and OER. As shown in Fig. 5a, after 5000 CV cycles at 5 mV s^{-1} , $\text{Ni}_3\text{S}_2@\text{MoS}_2/\text{FeOOH}$ shows negligible degradation for OER. Moreover, the over-

potential exhibits a loss of only 10 mV after 50 h chronopotentiometry test at a fixed current density of 10 mA cm^{-2} , as shown in Fig. 4b. The HER durability was evaluated by CV cycling test between the potential of $0.02 \sim -0.19 \text{ V}$ and chronopotentiometry test at a fixed current density of 10 mA cm^{-2} . As shown in Fig. 5c–d, no significant degradation can be observed after HER durability tests. These results demonstrate the good durability achieved on $\text{Ni}_3\text{S}_2@\text{MoS}_2/\text{FeOOH}$ heterostructure for both HER and OER.

3.6. Overall water splitting

Considering this superior electrocatalytic performance, an overall water splitting device was constructed using $\text{Ni}_3\text{S}_2@\text{MoS}_2/\text{FeOOH}$ heterostructure as both anode and cathode catalyst. Fig. 6a displays that the device only needs a small cell voltage of 1.57 V to deliver a

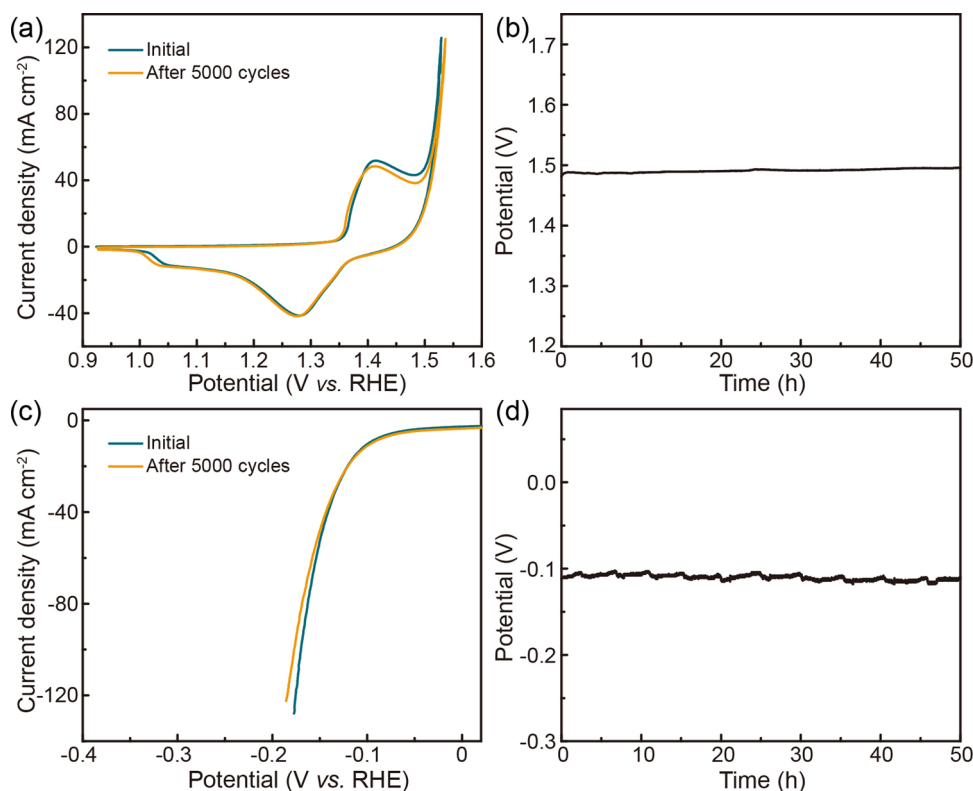


Fig. 5. (a) The 1st and 5000th CV curves at a scan rate of 5 mV s^{-1} , (b) OER chronopotentiometry curve at 10 mA cm^{-2} , (c) The 1st and 5000th HER polarization curves at a scan rate of 5 mV s^{-1} , (d) HER chronopotentiometry curve at 10 mA cm^{-2} , recorded on $\text{Ni}_3\text{S}_2@\text{MoS}_2/\text{FeOOH}$.

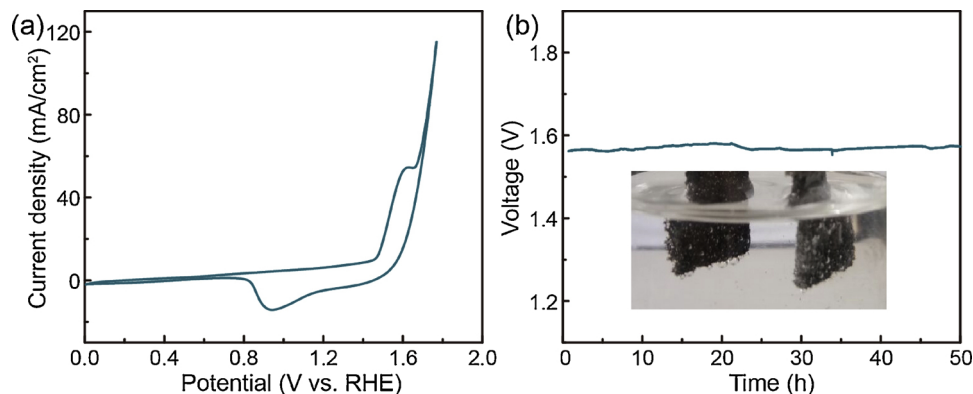


Fig. 6. (a) CV curve at a scan rate of 5 mV s^{-1} and (b) Chronopotentiometry curve at 10 mA cm^{-2} of overall water splitting using $\text{Ni}_3\text{S}_2@\text{MoS}_2/\text{FeOOH}$ as a bifunctional electrocatalyst for HER and OER.

current density of 10 mA cm^{-2} . It is lower than that of most of recently reported bifunctional electrocatalysts (Table S1). Moreover, the durability test at fixed current output reveals that the electrolyzer can function very well over a period of 50 h without appreciable cell voltage increase (Fig. 6b). SEM images show that the morphology of the electrode is preserved well after the durability test (Fig. S11). XPS results (Fig. S12) exhibit that the chemical states of Fe and O elements of $\text{Ni}_3\text{S}_2@\text{MoS}_2/\text{FeOOH}$ after stability tests are maintained well too. The absence of Ni^{2+} configuration and the positively shifted binding energy of Mo 3d spectra are due to the oxidation during the stability tests and the air exposure during measurements [50]. SEM and XPS results further prove the morphology and structure stability of $\text{Ni}_3\text{S}_2@\text{MoS}_2/\text{FeOOH}$ after HER and OER tests. These results suggest the potentials of $\text{Ni}_3\text{S}_2@\text{MoS}_2/\text{FeOOH}$ as a bifunctional electrocatalyst in practical overall water splitting.

4. Conclusion

In summary, to advance the MoS_2 -based catalysts in electrochemical water splitting, we successfully constructed a coupled core-shell $\text{Ni}_3\text{S}_2@\text{MoS}_2/\text{FeOOH}$ hybrid on Ni foam with Ni_3S_2 nanowire array cores and $\text{MoS}_2/\text{FeOOH}$ nanosheet shells. The morphological characterizations indicate that FeOOH nanosheet intimately coupled with MoS_2 nanosheets. XPS analyses reveal the clear electron redistribution from FeOOH to MoS_2 . Systematic investigations together with a series of control catalysts disclose that coupling FeOOH and MoS_2 can simultaneously promote the electrocatalytic activities for both OER and HER since electron-deficiency FeOOH is not only favorable for OER but also can accelerate water dissociation during HER. Consequently, the coupled $\text{Ni}_3\text{S}_2@\text{MoS}_2/\text{FeOOH}$ hybrid exhibits much improved electrocatalytic performance with lower overpotentials for alkaline OER and HER than most of reported MoS_2 -based electrocatalysts. The alkaline electrolyzer constructed with $\text{Ni}_3\text{S}_2@\text{MoS}_2/\text{FeOOH}$ as both anode and cathode can output a stable current density of 10 mA cm^{-2} at a small cell voltage of 1.57 V, demonstrating its capability as a bifunctional electrocatalyst for electrochemical overall water splitting. These results indicate that the present strategy coupling an OER-active electron-donative component with highly-active HER electrocatalysts may be effective for fabricating bifunctional electrocatalysts for electrochemical applications.

Acknowledgements

This work was supported by grants from National Natural Science Foundation of China (NNSFC No. 21673105, 21503102, 21701071), the Fundamental Research Funds for the Central University (LZUJBY-2017-106), the Science and Technology Program of Gansu Province of China (Grant No. 17JR5RA194), the National Postdoctoral Program for Innovative Talents (BX2001700250), and the project funded by China Postdoctoral Science Foundation (2017M620912). We wish to thank the Electron Microscopy Centre of Lanzhou University for the TEM/SEM measurements and structural analysis.

Appendix A. Supplementary data

Supplementary material related to this article can be found, in the online version, at doi:<https://doi.org/10.1016/j.apcatb.2018.12.019>.

References

- [1] H. Liang, A.N. Gandi, D.H. Anjum, X. Wang, U. Schwingenschlogl, H.N. Alshareef, Plasma-assisted synthesis of NiCoP for efficient overall water splitting, *Nano Lett.* 16 (2016) 7718–7725.
- [2] X. Zhong, Y. Sun, X. Chen, G. Zhuang, X. Li, J.-G. Wang, Mo doping induced more active sites in urchin-like $\text{W}_{18}\text{O}_{49}$ nanostructure with remarkably enhanced performance for hydrogen evolution reaction, *Adv. Funct. Mater.* 26 (2016) 5778–5786.
- [3] B. Dong, X. Zhao, G.-Q. Han, X. Li, X. Shang, Y.-R. Liu, W.-H. Hu, Y.-M. Chai, H. Zhao, C.-G. Liu, Two-step synthesis of binary Ni-Fe sulfides supported on nickel foam as highly efficient electrocatalysts for the oxygen evolution reaction, *J. Mater. Chem. A* 4 (2016) 13499–13508.
- [4] K. Mamtani, D. Jain, D. Dogu, V. Gustin, S. Gunduz, A.C. Co, U.S. Ozkan, Insights into oxygen reduction reaction (ORR) and oxygen evolution reaction (OER) active sites for nitrogen-doped carbon nanostructures (CN_x) in acidic media, *Appl. Catal. B: Environ.* 220 (2018) 88–97.
- [5] J. Luo, J.-H. Im, M.T. Mayer, M. Schreier, M.K. Nazeeruddin, N.-G. Park, S.D. Tilley, H.J. Fan, M. Grätzel, Water photolysis at 12.3% efficiency via perovskite photo-voltaics and earth-abundant catalysts, *Science* 345 (2014) 1593–1596.
- [6] H. Wang, H.-W. Lee, Y. Deng, Z. Lu, P.-C. Hsu, Y. Liu, D. Lin, Y. Cui, Bifunctional non-noble metal oxide nanoparticle electrocatalysts through lithium-induced conversion for overall water splitting, *Nat. Commun.* 6 (2015) 7261.
- [7] M. Risch, K.A. Stoerzinger, B. Han, T.Z. Regier, D. Peak, S.Y. Sayed, C. Wei, Z. Xu, Y. Shao-Horn, Redox processes of manganese oxide in catalyzing oxygen evolution and reduction: an in situ soft X-ray absorption spectroscopy study, *J. Phys. Chem. C* 121 (2017) 17682–17692.
- [8] B. Kang, X. Jin, S.M. Oh, S.B. Patil, M.G. Kim, S.H. Kim, S.-J. Hwang, An effective way to improve bifunctional electrocatalyst activity of manganese oxide via control of bond competition, *Appl. Catal. B: Environ.* 236 (2018) 107–116.
- [9] T. Tang, W.-J. Jiang, S. Niu, N. Liu, H. Luo, Q. Zhang, W. Wen, Y.-Y. Chen, L.-B. Huang, F. Gao, J.-S. Hu, Kinetically controlled coprecipitation for general fast synthesis of sandwiched metal hydroxide nanosheets/graphene composites toward efficient water splitting, *Adv. Funct. Mater.* 28 (2018) 1704594.
- [10] S. Niu, W.-J. Jiang, T. Tang, Y. Zhang, J.-H. Li, J.-S. Hu, Facile and scalable synthesis of robust $\text{Ni}(\text{OH})_2$ nanoplate arrays on NiAl foil as hierarchical active scaffold for highly efficient overall water splitting, *Adv. Sci.* 4 (2017) 1700084.
- [11] Z. Zhao, F. Qin, S. Kasiraju, L. Xie, M.K. Alam, S. Chen, D. Wang, Z. Ren, Z. Wang, L.C. Grabow, J. Bao, Vertically aligned $\text{MoS}_2/\text{Mo}_2\text{C}$ hybrid nanosheets grown on carbon paper for efficient electrocatalytic hydrogen evolution, *ACS Catal.* 7 (2017) 7312–7318.
- [12] M. Kim, S. Kim, D. Song, S. Oh, K.J. Chang, E. Cho, Promotion of electrochemical oxygen evolution reaction by chemical coupling of cobalt to molybdenum carbide, *Appl. Catal. B: Environ.* 227 (2018) 340–348.
- [13] S. Jing, L. Zhang, L. Luo, J. Lu, S. Yin, P.K. Shen, P. Tsiakaras, N-Doped porous molybdenum carbide nanobelts as efficient catalysts for hydrogen evolution reaction, *Appl. Catal. B: Environ.* 224 (2018) 533–540.
- [14] Y. Zhu, G. Chen, X. Xu, G. Yang, M. Liu, Z. Shao, Enhancing electrocatalytic activity for hydrogen evolution by strongly coupled molybdenum nitride/nitrogen-doped carbon porous nano-octahedrons, *ACS Catal.* 7 (2017) 3540–3547.
- [15] S. Dutta, A. Indra, Y. Feng, H. Han, T. Song, Promoting electrocatalytic overall water splitting with nanohybrid of transition metal nitride-oxynitride, *Appl. Catal. B: Environ.* 241 (2019) 521–527.
- [16] C. Tang, N. Cheng, Z. Pu, W. Xing, X. Sun, NiSe nanowire film supported on nickel foam: an efficient and stable 3D bifunctional electrode for full water splitting, *Angew. Chem. Int. Ed.* 54 (2015) 9351–9355.
- [17] X. Zhao, X. Li, Y. Yan, Y. Xing, S. Lu, L. Zhao, S. Zhou, Z. Peng, J. Zeng, Electrical and structural engineering of cobalt selenide nanosheets by Mn modulation for efficient oxygen evolution, *Appl. Catal. B: Environ.* 236 (2018) 569–575.
- [18] X. Wang, W. Li, D. Xiong, D.Y. Petrovykh, L. Liu, Bifunctional nickel phosphide nanocatalysts supported on carbon fiber paper for highly efficient and stable overall water splitting, *Adv. Funct. Mater.* 26 (2016) 4067–4077.
- [19] J. Xie, H. Zhang, S. Li, R. Wang, X. Sun, M. Zhou, J. Zhou, X.W. Lou, Y. Xie, Defect-rich MoS_2 ultrathin nanosheets with additional active edge sites for enhanced electrocatalytic hydrogen evolution, *Adv. Mater.* 25 (2013) 5807–5813.
- [20] P. Wang, X. Zhang, J. Zhang, S. Wan, S. Guo, G. Lu, J. Yao, X. Huang, Precise tuning in platinum-nickel/nickel sulfide interface nanowires for synergistic hydrogen evolution catalysis, *Nat. Commun.* 8 (2017) 14580.
- [21] N. Jiang, B. You, M. Sheng, Y. Sun, Electrodeposited cobalt-phosphorous-derived films as competent bifunctional catalysts for overall water splitting, *Angew. Chem. Int. Ed.* 54 (2015) 6251–6254.
- [22] R. Subbaraman, D. Tripkovic, D. Strmcnik, K.-C. Chang, M. Uchimura, A.P. Paulikas, V. Stamenkovic, N.M. Markovic, Enhancing hydrogen evolution activity in water splitting by tailoring $\text{Li}^+-\text{Ni}(\text{OH})_2\text{-Pt}$ interfaces, *Science* 334 (2011) 1256–1260.
- [23] J. Staszak-Jirkovsky, C.D. Malliakas, P.P. Lopes, N. Danilovic, S.S. Kota, K.C. Chang, B. Genorio, D. Strmcnik, V.R. Stamenkovic, M.G. Kanatzidis, N.M. Markovic, Design of active and stable Co-Mo-S_x chalcogenides as pH-universal catalysts for the hydrogen evolution reaction, *Nat. Mater.* 15 (2016) 197–203.
- [24] P.D. Tran, T.V. Tran, M. Orio, S. Torelli, Q.D. Truong, K. Nayuki, Y. Sasaki, S.Y. Chiam, R. Yi, I. Honma, J. Barber, V. Artero, Coordination polymer structure and revisited hydrogen evolution catalytic mechanism for amorphous molybdenum sulfide, *Nat. Mater.* 15 (2016) 640–646.
- [25] J. Xie, J. Zhang, S. Li, F. Grote, X. Zhang, H. Zhang, R. Wang, Y. Lei, B. Pan, Y. Xie, Controllable disorder engineering in oxygen-incorporated MoS_2 ultrathin nanosheets for efficient hydrogen evolution, *J. Am. Chem. Soc.* 135 (2013) 17881–17888.
- [26] R. Subbaraman, D. Tripkovic, K.C. Chang, D. Strmcnik, A.P. Paulikas, P. Hirunsit, M. Chan, J. Greeley, V. Stamenkovic, N.M. Markovic, Trends in activity for the water electrolyser reactions on 3d $\text{M}(\text{Ni}, \text{Co}, \text{Fe}, \text{Mn})$ hydr(oxy)oxide catalysts, *Nat. Mater.* 11 (2012) 550–557.
- [27] J. Zhang, T. Wang, P. Liu, S. Liu, R. Dong, X. Zhuang, M. Chen, X. Feng, Engineering water dissociation sites in MoS_2 nanosheets for accelerated electrocatalytic hydrogen production, *Energy Environ. Sci.* 9 (2016) 2789–2793.
- [28] Z. Zhuang, Y. Li, Z. Li, F. Lv, Z. Lang, K. Zhao, L. Zhou, L. Moskaleva, S. Guo, L. Mai,

- MoB/g-C₃N₄ interface materials as a schottky catalyst to boost hydrogen evolution, *Angew. Chem. Int. Ed.* 57 (2018) 496–500.
- [29] Y. Tang, H.J. Xu, J. Cao, C.F. Shan, B.K. Wang, P.X. Xi, W.S. Liu, MOF-derived hollow CoS decorated with CeO_x nanoparticles for boosting oxygen evolution reaction electrocatalysis, *Angew. Chem. Int. Ed.* 57 (2018) 8654–8658.
- [30] H. Lin, Z. Shi, S. He, X. Yu, S. Wang, Q. Gao, Y. Tang, Heteronanowires of MoC–Mo₂C as efficient electrocatalysts for hydrogen evolution reaction, *Chem. Sci.* 7 (2016) 3399–3405.
- [31] Y. Yang, K. Zhang, H. Lin, X. Li, H.C. Chan, L. Yang, Q. Gao, MoS₂–Ni₃S₂ heteronanorods as efficient and stable bifunctional electrocatalysts for overall water splitting, *ACS Catal.* 7 (2017) 2357–2366.
- [32] H. Zhu, J. Zhang, R. Yanzhang, M. Du, Q. Wang, G. Gao, J. Wu, G. Wu, M. Zhang, B. Liu, J. Yao, X. Zhang, When cubic cobalt sulfide meets layered molybdenum disulfide: a core-shell system toward synergistic electrocatalytic water splitting, *Adv. Mater.* 27 (2015) 4752–4759.
- [33] M. Zheng, J. Du, B. Hou, C.-L. Xu, Few-layered Mo_(1–x)W_xS₂ hollow nanospheres on Ni₃S₂ nanorod heterostructure as robust electrocatalysts for overall water splitting, *ACS Appl. Mater. Interfaces* 9 (2017) 26066–26076.
- [34] W.D. Chemelewski, H.C. Lee, J.F. Lin, A.J. Bard, C.B. Mullins, Amorphous FeOOH oxygen evolution reaction catalyst for photoelectrochemical water splitting, *J. Am. Chem. Soc.* 136 (2014) 2843–2850.
- [35] G. Chen, H. Agren, T.Y. Ohulchanskyy, P.N. Prasad, Light upconverting core-shell nanostructures: nanophotonic control for emerging applications, *Chem. Soc. Rev.* 44 (2015) 1680–1713.
- [36] Z. Chen, D. Cummins, B.N. Reinecke, E. Clark, M.K. Sunkara, T.F. Jaramillo, Core-Shell MoO₃–MoS₂ nanowires for hydrogen evolution: a functional design for electrocatalytic materials, *Nano Lett.* 11 (2011) 4168–4175.
- [37] D. Wang, H.L. Xin, R. Hovden, H. Wang, Y. Yu, D.A. Muller, F.J. DiSalvo, H.D. Abruna, Structurally ordered intermetallic platinum-cobalt core-shell nanoparticles with enhanced activity and stability as oxygen reduction electrocatalysts, *Nat. Mater.* 12 (2013) 81–87.
- [38] X. Xiong, B. Zhao, D. Ding, D. Chen, C. Yang, Y. Lei, M. Liu, One-step synthesis of architectural Ni₃S₂ nanosheet-on-nanorods array for use as high-performance electrodes for supercapacitors, *NPG Asia Mater.* 8 (2016) e300.
- [39] J.X. Feng, H. Xu, Y.T. Dong, S.H. Ye, Y.X. Tong, G.R. Li, FeOOH/Co/FeOOH hybrid nanotube arrays as high-performance electrocatalysts for the oxygen evolution reaction, *Angew. Chem. Int. Ed.* 55 (2016) 3694–3698.
- [40] J.X. Feng, S.H. Ye, H. Xu, Y.X. Tong, G.R. Li, Design and synthesis of FeOOH/CeO₂ heterolayered nanotube electrocatalysts for the oxygen evolution reaction, *Adv. Mater.* 28 (2016) 4698–4703.
- [41] J. Wang, D. Chao, J. Liu, L. Li, L. Lai, J. Lin, Z. Shen, Ni₃S₂@MoS₂ core/shell nanorod arrays on Ni foam for high-performance electrochemical energy storage, *Nano Energy* 7 (2014) 151–160.
- [42] Q. Yao, Z.-H. Lu, W. Huang, X. Chen, J. Zhu, High Pt-like activity of the Ni–Mo/graphene catalyst for hydrogen evolution from hydrolysis of ammonia borane, *J. Mater. Chem. A* 4 (2016) 8579–8583.
- [43] J. Chen, J. Xu, S. Zhou, N. Zhao, C.-P. Wong, Amorphous nanostructured FeOOH and Co–Ni double hydroxides for high-performance aqueous asymmetric supercapacitors, *Nano Energy* 21 (2016) 145–153.
- [44] X. Dai, K. Du, Z. Li, M. Liu, Y. Ma, H. Sun, X. Zhang, Y. Yang, Co-doped MoS₂ nanosheets with the dominant CoMoS phase coated on carbon as an excellent electrocatalyst for hydrogen evolution, *ACS Appl. Mater. Interfaces* 7 (2015) 27242–27253.
- [45] Z. Pu, Q. Liu, A.M. Asiri, Y. Luo, X. Sun, Y. He, 3D macroporous MoS₂ thin film: in situ hydrothermal preparation and application as a highly active hydrogen evolution electrocatalyst at all pH values, *Electrochim. Acta* 168 (2015) 133–138.
- [46] Y. Zhao, K. Kamiya, K. Hashimoto, S. Nakanishi, In situ CO₂-emission assisted synthesis of molybdenum carbonitride nanomaterial as hydrogen evolution electrocatalyst, *J. Am. Chem. Soc.* 137 (2015) 110–113.
- [47] G.-F. Chen, Y. Luo, L.-X. Ding, H. Wang, Low-voltage electrolytic hydrogen production derived from efficient Water and ethanol oxidation on fluorine-modified FeOOH anode, *ACS Catal.* 8 (2018) 526–530.
- [48] N. Cheng, Q. Liu, A.M. Asiri, W. Xing, X. Sun, A Fe-doped Ni₃S₂ particle film as a high-efficiency robust oxygen evolution electrode with very high current density, *J. Mater. Chem. A* 3 (2015) 23207–23212.
- [49] W.-J. Jiang, S. Niu, T. Tang, Q.-H. Zhang, X.-Z. Liu, Y. Zhang, Y.-Y. Chen, J.-H. Li, L. Gu, L.-J. Wan, J.-S. Hu, Crystallinity-modulated electrocatalytic activity of a nickel(II) borate thin layer on Ni₃B for efficient water oxidation, *Angew. Chem. Int. Ed.* 56 (2017) 6572–6577.
- [50] J. Zhang, T. Wang, D. Pohl, B. Rellinghaus, R. Dong, S. Liu, X. Zhuang, X. Feng, Interface engineering of MoS₂/Ni₃S₂ heterostructures for highly enhanced electrochemical overall-Water-splitting activity, *Angew. Chem. Int. Ed.* 55 (2016) 6702–6707.
- [51] K. Yan, Y. Lu, Direct growth of MoS₂ microspheres on Ni foam as a hybrid nanocomposite efficient for oxygen evolution reaction, *Small* 12 (2016) 2975–2981.
- [52] D. Xiong, Q. Zhang, W. Li, J. Li, X. Fu, M.F. Cerqueira, P. Alpuim, L. Liu, Atomic-layer-deposited ultrafine MoS₂ nanocrystals on cobalt foam for efficient and stable electrochemical oxygen evolution, *Nanoscale* 9 (2017) 2711–2717.
- [53] T.-N. Ye, L.-B. Lv, M. Xu, B. Zhang, K.-X. Wang, J. Su, X.-H. Li, J.-S. Chen, Hierarchical carbon nanopapers coupled with ultrathin MoS₂ nanosheets: highly efficient large-area electrodes for hydrogen evolution, *Nano Energy* 15 (2015) 335–342.
- [54] M. Caban-Acevedo, M.L. Stone, J.R. Schmidt, J.G. Thomas, Q. Ding, H.C. Chang, M.L. Tsai, J.H. He, S. Jin, Efficient hydrogen evolution catalysis using ternary pyrite-type cobalt phosphosulfide, *Nat. Mater.* 14 (2015) 1245–1251.
- [55] X. Yan, L. Tian, S. Atkins, Y. Liu, J. Murovchick, X. Chen, Converting CoMoO₄ into CoO/MoO_x for overall water splitting by hydrogenation, *ACS Sustain. Chem. Eng.* 4 (2016) 3743–3749.
- [56] X. Yan, L. Tian, M. He, X. Chen, Three-dimensional crystalline/amorphous Co/Co₃O₄ core/shell nanosheets as efficient electrocatalysts for the hydrogen evolution reaction, *Nano Lett.* 15 (2015) 6015–6021.
- [57] A. Grimaud, K.J. May, C.E. Carlton, Y.L. Lee, M. Risch, W.T. Hong, J. Zhou, Y. Shao-Horn, Double perovskites as a family of highly active catalysts for oxygen evolution in alkaline solution, *Nat. Commun.* 4 (2013) 2439.
- [58] T. Tang, W.J. Jiang, S. Niu, N. Liu, H. Luo, Y.Y. Chen, S.F. Jin, F. Gao, L.J. Wan, J.S. Hu, Electronic and morphological dual modulation of cobalt carbonate hydroxides by Mn doping toward highly efficient and stable bifunctional electrocatalysts for overall water splitting, *J. Am. Chem. Soc.* 139 (2017) 8320–8328.